



HAL
open science

Impact driving of monopiles in centrifuge: effect on the lateral response in sand

Semaan Maatouk, Matthieu Blanc, Luc Thorel

► To cite this version:

Semaan Maatouk, Matthieu Blanc, Luc Thorel. Impact driving of monopiles in centrifuge: effect on the lateral response in sand. *International Journal of Physical Modelling in Geotechnics*, 2021, 14 p. 10.1680/jphmg.21.00035 . hal-03483583

HAL Id: hal-03483583

<https://hal.science/hal-03483583>

Submitted on 16 Dec 2021

HAL is a multi-disciplinary open access archive for the deposit and dissemination of scientific research documents, whether they are published or not. The documents may come from teaching and research institutions in France or abroad, or from public or private research centers.

L'archive ouverte pluridisciplinaire **HAL**, est destinée au dépôt et à la diffusion de documents scientifiques de niveau recherche, publiés ou non, émanant des établissements d'enseignement et de recherche français ou étrangers, des laboratoires publics ou privés.

Impact driving of monopiles in centrifuge: effect on the lateral response in sand

Semaan Maatouk¹

PhD candidate, Laboratory of Centrifuges for Geotechnics, Department GERS, Gustave Eiffel University, Bouguenais, France (Orcid:0000-0003-2125-1020)

Matthieu Blanc²

Researcher, Laboratory of Centrifuges for Geotechnics, Department GERS, Gustave Eiffel University, Bouguenais, France (Orcid:0000-0003-0603-487X)

Luc Thorel³

Senior researcher, Laboratory of Centrifuges for Geotechnics, Department GERS, Gustave Eiffel University, Bouguenais, France (Orcid:0000-0002-0218-4144)

Corresponding author: semaan.maatouk@univ-eiffel.fr, +33 2 40 84 59 15

Submitted: 10/05/2021

Accepted: 28/07/2021

Number of words: 5736

Number of figures: 10

Number of tables: 7

Ahead of print in International Journal of Physical Modelling in Geotechnics, Ice Publishing. Published online : 06/09/2021
<https://doi.org/10.1680/jphmg.21.00035>

Abstract

This study examines the influence of impact-driven installation on the subsequent horizontal monotonic response of small-scale monopiles by using a large-beam geotechnical centrifuge at 100g. A special device including small-scale hammer was developed to install open-ended monopiles with 50 mm in diameter to an embedment depth of 250 mm in flight, and then to apply lateral loading on the monopile head without stopping the centrifuge. The horizontal global and local responses of the monopiles were investigated for two methods of installation: impact driven at 100g, and monotonically jacked at 1g into saturated dense sand. The results highlighted two main features. (i) The effect of impact driving was pronounced for small amplitudes of horizontal loading. With regard to the conditions of serviceability, the in-flight installation increased the secant stiffness by about 3 times compared with the 1g installation. For large amplitude of displacement, the lateral capacity increased by 1.3 times. (ii) The experimental p - y curves obtained from the in-flight impact-driven installation remained smoother than those predicted by using offshore standards, but were similar to them.

Keywords: centrifuge modelling; pile and piling; sand

Notation

C_u	coefficient of uniformity [dimensionless]
D	monopile outer diameter [m]
d_{50}	average diameter of sand grains [mm]
EI	monopile bending stiffness [N m ²]
G	monopile shear modulus [GPa]
g	Earth gravitational acceleration [m/s ²]
H	horizontal load [MN]
H_G	horizontal load at the ground level [MN]
h	ram drop height [m]
h_a	anvil height [m]
k	lateral secant stiffness
L	monopile embedment length [m]
l	monopile length [m]
l_e	load eccentricity [m]
M	bending moment [MN m]
M_G	bending moment at ground level [MN m]

m	ram mass [kg]
N	g level [dimensionless]
n	hammer blows [dimensionless]
p	soil reaction [MN/m]
R_N	radius of the application of the Centrifuge acceleration [m]
S	shear force [MN]
s	monopile settlement [m]
s_i	monopile settlement for the hammer impact $n^\circ i$ [m]
t	monopile wall thickness [m]
y	monopile lateral deflection [m]
y_G	monopile lateral deflection at ground level [m]
z	depth coordinate [m]
ε	monopile normal strain [$\mu\text{m}/\text{m}$]
ϵ	energy delivered to drive the monopile [MJ]
Φ	angle of friction [$^\circ$]
θ	rotation of monopile neutral axis [$^\circ$]
θ_G	rotation of monopile neutral axis at ground level [$^\circ$]
κ	Timoshenko shear coefficient [dimensionless]
ξ	applied cumulated driving energy [MJ]
ξ^N	simplified cumulated driving energy [MJ]
$\rho_{d\text{max}}$	maximum dry density [g/cm^3]
$\rho_{d\text{min}}$	minimum dry density [g/cm^3]
ρ_s	dry density of solid particles [g/cm^3]
Δ	improvement of the monopile resistance/secant stiffness [%]

1 1 Introduction

2 Offshore wind farms have grown in number in the last few decades in the course of efforts to
3 produce clean and renewable energy. Monopiles are the prevalent foundations for offshore wind
4 turbines in shallow coastal waters (e.g. Dupla *et al.*, 2019). They are commonly installed in
5 dense sand using a dynamic method: the so-called impact driving. Over their design service life,
6 the monopiles are subjected to horizontal loading due to winds, currents, and waves. This is
7 why offshore monopiles are designed to withstand lateral loads and overturning moments.

8

9 To investigate the lateral response of impact-driven monopiles in sandy environments, two
10 experimental methods have been proposed in the literature: in-situ testing and laboratory
11 testing. Field tests can be performed onshore on monopiles of different sizes. For example,
12 monotonic lateral tests were conducted on driven monopiles of small-to-medium diameters
13 (0.273–2 m) under the framework of the Pile Soil Analysis (PISA) joint industry project (McAdam
14 *et al.*, 2020; Burd *et al.*, 2020a). Small-scale model tests have been conducted in laboratories,
15 either at 1g (e.g. Abadie *et al.*, 2019) or with enhanced stress, by accelerating the centrifuge
16 (e.g. Klinkvort, 2012 ; Fan *et al.*, 2019). Centrifuge models tested in macro-gravity undergo
17 similar stress fields to full-scale prototypes. Hence, by using the scaling laws of physical
18 modelling (e.g. Garnier *et al.*, 2007), the response of the monopile model can be compared to
19 that of the prototype. Like the in-situ conditions, the method of installation (e.g. for displacement
20 or non-displacement piles) plays an important role on the pile behaviour. The generated stress
21 field changes significantly depending on the method of pile installation used: whether driven or
22 wished in place. In the same way in the centrifuge, the stress field generated during installation
23 at 1g is different from that when installation is performed in flight. The horizontal response of the
24 model of the pile obtained through the centrifuge is weaker than that predicted by standards
25 such as the DNVGL (2016) (e.g. Bayton and Black (2016), Choo and Kim (2016), El Haffar
26 (2018)). One reason for this is that clean sand is used in centrifuge modelling, and is
27 significantly different than that used in situ. Another reason, reported by Fan *et al.* (2019), is that
28 driving the monopile in flight increases the stiffness of the horizontal response as well as the
29 lateral resistance of soil. As highlighted by Bayton and Black (2016), the experimental response

30 of the monopile in this case is expected to be closer to the design standards. A miniature
31 monopile-driving hammer can thus be developed to simulate the method of 'in-flight' installation
32 during centrifuge model tests. The three main characteristics of hammering are its frequency
33 (blow rate), the mass of the ram, and the drop height. A list of different in-flight hammers
34 developed to drive piles and monopiles in centrifuges (updated from Levacher *et al.*, 2008) is
35 provided in Table 1.

36

37 Several studies have focused on the lateral responses of piles and monopiles installed in the
38 centrifuge by using different methods. Kim *et al.* (2004) have highlighted different lateral
39 responses of piles installed as wished in place, and by being driven at 1g by using different
40 energies. Furthermore, Dyson and Randolph (2001), and Klinkvort (2012) have studied the
41 effects of monotonically jacked and impact-driven in-flight installations on the responses of the
42 lateral pile and the monopile. However, these tests required stopping the centrifuge to mount
43 the lateral loading apparatus, which led to a loss of the state of soil post installation. Fan *et al.*
44 (2021a) showed by using advanced numerical modelling that the post-installation state of soil,
45 including horizontal stresses and the void ratio, is altered by the process of installation of the
46 monopile in dry and sandy environments. The post-installation state of soil therefore needs to
47 be retained in centrifuge modelling. This was achieved by Fan *et al.* (2019), who performed
48 three direct monotonic push-over tests without stopping the centrifuge on a 50-mm monopile
49 model monotonically jacked at 1g and 100g, and impact-driven at 100g into dry sand of medium
50 density to a depth of 3.1D. Fan *et al.* (2019) claimed that the global lateral response of the
51 monopile was significantly influenced by the method of installation, and this was numerically
52 confirmed by Fan *et al.* (2021b). Fan *et al.* (2021b) also revealed that the effect of the method of
53 installation on the lateral response is affected by the initial density of soil, driving distance,
54 geometry of the monopile, and the level of stress and eccentricity of the load.

55

56 This study develops an experimental device that can carry out, in centrifuge at 100g, the impact-
57 driven installation of an instrumented monopile with 50 mm in diameter into a 250 mm (5D)
58 embedding, followed by horizontal loading. Test was conducted to verify the performance of the

59 set-up, and to better understand the effect of the impact-driven installation of the monopile on its
60 subsequent global and local lateral response in saturated dense sand.

61 **2 Development of the experimental device**

62 To study the influence of the hammering installation method in centrifuge on the horizontal
63 response of the monopile, a special device was developed. The goal of development was to
64 drive the monopile in flight and then apply horizontal loading without stopping the centrifuge to
65 maintain the states of stress that had been induced by the installation of the monopile
66 beforehand. This enabled the better modelling of the post-installation stress field. The device
67 (Figure 1) had two main axes. (i) Vertically, an electric motor was fixed at the top on a hydraulic
68 actuator; it was positioned on I-shaped supporting beams, and was used to control the hammer
69 (shown in Figure 2(a)). (ii) Horizontally, an electro-mechanical actuator was fixed on a 'T-
70 metallic' support beam to laterally load the monopile. These actuators were equipped with
71 external force sensors and displacement sensors (Table 2). The electro-mechanical hammer
72 was based on the principle of the combined spin-upward movement of the ram before free-fall.

73

74 A 0.166-kg steel anvil was fixed over the head of the aluminium monopile to avoid damaging it
75 at the moment of shock. The falling mass included wing-shaped ram weights, and two
76 diametrically opposed cylinder bearings were wrapped around them. These two bearings rested
77 on a fixed wave-shaped ram support that allowed the ram to free-fall to a height of 25 mm to hit
78 the anvil and then move back up the ram with a constant slope through rotation. The shape of
79 the ram support thus enabled the impact driving of the monopile with two blows per turn. The
80 ram support, driving guide, and housing of the hammer were supported by the vertical actuator
81 to follow the descent of the monopile. Inside the hollow rod of the hydraulic actuator, a
82 connection bar that linked the vertical fork to the electric motor enabled its rotation. This rotating
83 fork allowed for both the vertical translation (rise up and free-fall) and rotation of the free ram.
84 The details of the miniature hammer are presented in Figure 2(b).

85

86 As the monopile penetrated the soil, the vertical actuator followed it downward while maintaining
87 a specified drop height for impact through a vertical laser displacement transducer (Table 2) that

88 measured the distance to the target fixed on the monopile shaft (as shown in Figure 2(a)). A
89 driving guide fixed below the hammer also ensured the verticality of the monopile during
90 installation. During the hammering, the monopile slightly spun about its vertical axis. This was
91 avoided by using a steel rod that diametrically crossed the monopile 25 mm from its head and
92 hung on the foot of the driving guide. A slight gap was provided between the hole of the
93 monopile and the steel rod to avoid excessive pressure from being generated inside the
94 monopile during hammering.

95

96 Once the monopile had reached the desired embedment depth, the electric motor spinning the
97 ram was stopped. The vertical actuator was then lifted up to leave the monopile inside the sand
98 sample. The possible translation and rotation of the monopile after installation in the vertical
99 plan of the horizontal loading were measured by using two horizontal laser displacement
100 transducers positioned in front of the horizontal actuator (Figure 2(a)). A maximum slight
101 translation of 1 mm and rotation of 0.57° were observed in the direction opposite to that of the
102 lateral loading.

103

104 Following this, without stopping the centrifuge to maintain the stress state, lateral loading was
105 applied to the centre of the cross-section of the monopile by pushing the steel rod that crossed
106 the monopile perpendicularly to the direction of loading by using a fork attached to the horizontal
107 electro-mechanical actuator. A photograph of the horizontal loading set-up after unloading the
108 monopile and stopping the centrifuge is presented in Figure 3.

109

110 The hydraulic vertical actuator, horizontal electric actuator, and electric motor were together
111 connected to a MOOG© test controller placed near the axis of the centrifuge. The controller
112 contained three servo-loops working at a frequency of up to 1.6 kHz that could be connected to
113 various types of sensor (force, displacement, and acceleration).

114 **3 Centrifuge model test**

115 The tests were performed in a geotechnical centrifuge facility, with a beam of radius 5.5 m, at
116 the Gustave Eiffel University, Nantes campus, France (formerly IFSTTAR or LCPC). The set-up

117 was installed in the swinging basket of the centrifuge (Figure 1(b)), where the total available
118 vertical height was 2110 mm. The tests were carried out at 100 times the Earth's gravity (N
119 $=100$) on a large monopile model of diameter $D = 50$ mm embedded over $5D$ into water-
120 saturated dense sand, and was horizontally loaded at an altitude of $l_e = 5D$ from the ground
121 level. The level of g was applied at a depth of 83 mm from the surface of soil (i.e. $L/3$),
122 corresponding to a radius R_N of 5.2 m from the axis of the centrifuge.

123 **3.1 Sand model**

124 The sand sample was reconstituted by using the raining deposition technique (Garnier, 2001),
125 which yields a homogenous specimen and has good repeatability (Ternet, 1999). Poorly graded
126 NE34 Fontainebleau sand was deposited from an automatic hopper that moved back and forth
127 at a constant horizontal speed of 10 cm/s. The sand fell at a constant height of 70 cm through a
128 3-mm-wide slot to produce uniform sand rain over a strongbox with internal dimensions of 1200
129 (length) by 800 (width) by 360 (depth) mm³. The resulting density was 1.682 g/cm³, with a
130 coefficient of variation of 0.24%, i.e. $82\% \pm 1.4\%$ of relative density, and was based on seven
131 calibrated boxes spread at the bottom of the strongbox ($C_u = 1.53$, $d_{50} = 0.21$ mm, $\Phi = 38^\circ$, $\rho_s =$
132 2.65 g/cm³, $\rho_{dmin} = 1.434$ g/cm³, $\rho_{dmax} = 1.746$ g/cm³ (Klinkvort, 2018)). Following the pluviation
133 of sand, a 120-mm-high raiser (Figure 1) was placed over the strongbox. The sample was then
134 saturated by tap water through vertical rising flow using four draining channels located at the
135 bottom of the specimen (Figure 1(a)). To avoid scale effects between diffusion and the dynamic
136 phenomena, the sand mass can be saturated by using a fluid with a viscosity of 100 cst (Kutter,
137 1994). This was not done in this study. Only the impact of the method of installation on the
138 horizontal response of the monopile was studied here. The final water level was 40 mm above
139 the surface of sand at 1g to ensure that the sand remained fully saturated at 100g. The effective
140 unit weight of the saturated sand was 10.26 kN/m³.

141 **3.2 Monopile model**

142 An open-ended tubular aluminium 2017A tube (Figure 4(a)) of length $l = 525$ mm, external
143 diameter $D = 50$ mm, and a 2.5 mm-thick wall (t) was used. Two optical fibres, described below,
144 were embedded into a tube of suitable thickness (thicker than the minimum thickness required

145 according to API (2007)) while respecting the scale factor of flexural rigidity EI . Aluminium tubes
146 are commonly used in geotechnical centrifuges (e.g. Rosquoët *et al.*, 2007), and they do not
147 rust in a saturated sand. The geometry and the mechanical characteristics of the model
148 monopile are presented in Table 3.

149

150 The roughness of the pile, normalised by the average grain size as introduced by Uesugi and
151 Kishida (1986), was 0.015 (less than 0.1). Therefore, it was considered to be smooth according
152 to Garnier and Konig (1998), and the normalised surface roughness is typically within the range
153 of 0.02 to 0.03 of a standard offshore pile, as reported De Nicola and Randolph (1997).

154

155 To avoid particle-size effect on the horizontal response of the monopile, a series of 'modelling of
156 models' performed by Remaud (1999) have suggested a ratio of pile to grain diameter D/d_{50}
157 greater than 60. In addition, the ratio of the thickness of the wall to mean particle size t/d_{50}
158 needed to be at least 10 (De Nicola, 1996). Both criteria were verified ($D/d_{50} = 238$, $t/d_{50} = 12$) by
159 using Fontainebleau NE34 sand and the geometry of the chosen monopile.

160 **3.3 Monopile instrumentation**

161 The model monopile was instrumented with two diametrically opposed optical fibres, each with a
162 diameter of 200 μm , glued into two semi-cylindrical grooves with a radius of 0.5 mm (1/5 of the
163 thickness of the wall) as shown in Figure 4(b). The position of the two optical fibres, in extension
164 and compression sides, compensated for the effect of temperature on the resulting bending
165 moment. Within each fibre, 10 equally distributed fibre Bragg gratings (FBGs) were integrated
166 from the ground level to the pile base over a span of 225 mm, as shown in Figure 4(a). The
167 details of this instrumented model monopile and its calibration have been provided by Li *et al.*
168 (2020).

169

170 In an open-ended monopile, plugging may occur during installation to change the response. For
171 this purpose, the internal height of the soil column during monopile installation was measured by
172 using a potentiometric position sensor (Table 2) fixed by an aluminium support on the steel rod

173 inside the monopile. The tip of the sensor rod was 160 mm from the monopile base before
 174 installation.

175 **3.4 Hammering procedure**

176 The monopile restricted within the driving guide penetrated a few millimetres into the sand
 177 before spinning the centrifuge, and then continued to penetrate into it as gravity was increased.
 178 At 100g, the displacement of the vertical hydraulic actuator holding the hammer was controlled
 179 to maintain the required height at which the ram was dropped based on the vertical
 180 displacement of the laser. The electric motor was then activated and impact driving was
 181 initiated. In general, the driving energy input into the system can be varied according to the drop
 182 height and the mass of the ram of the hammer. In this case, the ram weighed 0.164 kg, and a
 183 drop height of 20 mm was chosen.

184 The driving energy per stroke increased with the depth of penetration as the centrifugal
 185 acceleration varied with the radius (i.e. with the altitude of the anvil). Because the head of the
 186 anvil was located at an altitude corresponding to 88.65g before the monopile was driven, and at
 187 one corresponding to 92.84g at the end of the hammering, the delivered energy chosen to drive
 188 the model monopile down to the desired depth varied from 2.85 J to 2.99 J (2.85 MJ to 2.99 MJ
 189 at prototype scale, with $N = 100$). The maximum rotational speed of the electric motor was 900
 190 rounds per minute, but it was fixed in this case to 150 rpm, which corresponded to five blows
 191 per second.

192

193 Figure 5 shows the cumulative number of blows of the hammer (n), the simplified cumulative
 194 driving energy ξ^N (without variation in the gradient of centrifuge acceleration during hammering),
 195 and the applied driving energy ξ (with variations) versus the normalised settlement of the
 196 monopile. In both cases, the driving energy (ϵ_{i+1}^N and ϵ_{i+1}) and the cumulative driving energy
 197 (ξ_{i+1}^N and ξ_{i+1}) at the $(i+1)^{\text{th}}$ blow in 'MJ' were calculated at prototype scale as follows:

$$\left\{ \begin{array}{l} \epsilon_{i+1}^N = mghN \\ \epsilon_{i+1} = \epsilon_{i+1}^N \frac{R_N - \frac{L}{3} - l - h_a + s_i}{R_N} \end{array} \right. \quad (1)$$

$$\begin{cases} \xi_{i+1}^N = n_{i+1} \epsilon_{i+1}^N \\ \xi_{i+1} = \xi_i + \epsilon_{i+1} \end{cases} \quad (2)$$

198 where all the length-related parameters were at model scale in 'm', and the height of the anvil h_a
 199 = 0.014 m. The initial depth s_0 , around $0.65D$, represented the monopile penetration under its
 200 own weight before being driven. The number of blows as well as the delivered energy required
 201 per unit meter of penetration increased with the penetration depth, as expected. A total of 3846
 202 blows were needed to drive the monopile to an embedment depth of $5D$. The maximum
 203 difference in cumulative energy between the methods of calculation was 12.8%. During this
 204 installation, the vertical displacement sensor inside the monopile indicated that no plugging had
 205 occurred.

206 **3.5 Horizontal loading procedure**

207 After installation, the hammer and the vertical actuator were lifted up in flight to create the
 208 required clearance around the head of the monopile for the lateral loading phase. Lateral
 209 loading was applied by pushing the steel rod, positioned perpendicularly with respect to the
 210 plane of the optical fibres at $l_e = 250$ mm (i.e. $5D$), above the ground level. This was achieved by
 211 moving the horizontal electro-mechanical actuator to 50 mm (i.e. $1D$) at a controlled rate of 0.1
 212 mm/s. During the loading phase, the lateral load at the electro-mechanical actuator was
 213 recorded by using a horizontal load cell. The horizontal deflections of the monopile at 60 mm
 214 and at 220 mm above the ground level were measured by using two horizontal laser
 215 displacement transducers. These transducers, positioned in front of the actuator, were mounted
 216 on a bracket attached to the bottom of the I-beams (as shown in Figures 2(a) and 3).

217

218 The measurements of the sensors were recorded by a data acquisition system (QuantumX
 219 MX1615 from HBK) placed in the swinging basket of the centrifuge. The FS22DI Industrial
 220 BraggMETER Interrogator box from HBK, which can record the reflected peak wavelength in
 221 Bragg optical fibres to allow for the measurement of the normal strain, was placed near the axis
 222 of the centrifuge. These two data acquisition devices were connected to the same local ethernet
 223 network at a recording frequency of 100 Hz.

224 4 Impact of driving monopile on horizontal response

225 For comparison with the impact-driven installation (called 'ID100g' here), a reference monopile
226 monotonically jacked at 1g (called 'J1g') was first tested in the same strongbox. The 1g
227 installation was performed at a constant displacement rate of 1 mm/s to a depth of $5D$. Then,
228 centrifuge acceleration was applied at 100g only in the lateral loading phase (detailed in Section
229 3.5). As a result, the stress states of soil generated around the monopiles were different from
230 those obtained after impact driving at 100g. Both tests were carried out at $8D$ (i.e. 400 mm) from
231 the walls of the strongbox, perpendicular to the plane of horizontal loading, to minimise
232 boundary-related issues. In this section, all results are presented at an equivalent prototype
233 scale.

234 4.1 Comparison of global behaviour

235 Direct measurements of the ground-level displacement and rotation, and force are not feasible
236 in the centrifuge. These data can be obtained by modelling the above-ground structure as a
237 beam according to Timoshenko's theory (Astley (1992)) by using two displacement transducers
238 positioned at different elevations (Mayall, 2019; Fan *et al.*, 2019). However, this approach did
239 not yield sufficiently accurate results for two reasons. i) There were uncertainties in
240 displacements of small amplitude at the bottom laser displacement transducer (as shown in
241 Figure 9). ii) The distance between these transducers was too short to yield accurate values of
242 rotation. Moreover, the recommended use of inclinometers in field tests along the embedded
243 depth (Burd *et al.*, 2020a; Byrne *et al.*, 2020; McAdam *et al.*, 2020) was not possible in the
244 centrifuge. This is why the procedure developed by Li *et al.* (2020) was implemented: The
245 centre of rotation of the monopile was used to infer its horizontal displacement and rotation at
246 the ground level. This method is detailed in the next sub-section as it involves strain
247 measurements along the embedded depth of the monopile.

248

249 At ground level, the bending moment M_G and horizontal load H_G are plotted, in Figure 6(a) and
250 Figure 6(b) respectively, against the rotation of the monopile about the neutral axis θ_G and its
251 normalised deflection y_G/D for both methods of installation: by impact driving at 100g (ID100g),

252 and monotonically jacked at 1g (J1g). In both tests, two trends/behaviours were observed. i)
253 Initially, for small amplitudes of loading, the lateral resistance increased until $\theta_G = 0.7^\circ$ or $y_G =$
254 $0.03D$ (i.e. 0.15 m). ii) Then, this increase became less pronounced. For the same y_G/D or θ_G ,
255 H_G or M_G was always greater for ID100g than for J1g. Figure 6(a) and Figure 6(b) also show the
256 improvement (Δ) brought about by the in-flight impact-driven installation. This improvement
257 corresponded to the difference in the resistance of the monopile between the tests as
258 normalised by the lateral resistance in the J1g test. The improvement due to the hammering
259 was much more pronounced during the first phase of the tests (until $\theta_G = 0.7^\circ$). In the second
260 phase, the difference between the resistance of the tests remained constant. As the resistance
261 increased during loading, the improvement, due to the in-flight installation decreased until
262 reaching a plateau for high amplitudes of loading far from the domain of serviceability. The
263 findings are in accordance with the results obtained by Fan *et al.* (2019). To better understand
264 these trends, authors focus on the local behaviour of the monopile instrumented by optical strain
265 gauges.

266 **4.2 Comparison of local behaviour**

267 The resistance of the monopile to lateral loading depends on several mechanisms of interaction
268 (Byrne *et al.*, 2017): the horizontal soil reactions p , the interface shear along the monopile shaft,
269 and the shear and moment resistances at its base.

270 **4.2.1 Axial strains**

271 Under lateral loading, the monopile bent to induce axial strains in optical fibres located at the
272 extremities of the cross-section in the direction of loading. For both tests ID100g and J1g, these
273 local strains as measured by FBGs are plotted in Figure 7 along the depth of the monopile for
274 four loading states, corresponding to $M_G = 100, 200, 300,$ and 400 MN.m. As the applied
275 loading increased, normal strains within the monopile increased as well. Under the same value
276 of M_G , normal strains in both tests increased with depth until reaching a maximum at the fourth
277 FBG ($z = 1.5D$), below which they continued to decrease progressively to almost zero near the
278 monopile base. However, the ID100g test featured amplitudes of axial strain lower than those of
279 the J1g test. At the same depth, asymmetry was noted between compression and tension, and

280 became more significant at the monopile base. This asymmetrical behaviour has been reported
281 by Doherty *et al.* (2015) and McAdam *et al.* (2020) in lateral field tests on steel piles driven into
282 dense sand. However, the reason for this was not identified. It may have occurred due to the
283 localisation of strain along the boundaries of the monopile, as its slenderness ratio was too low
284 to consider the monopile to be an ‘idealised flexible beam’.

285 4.2.2 Bending moments

286 After calibration of the FBGs (Li *et al.*, 2020), bending moments at different depths of the
287 monopile were calculated, as shown in Equation 3, based on the average values of the tensile
288 and compressive strains ϵ_{avg} by using Euler–Bernoulli beam theory:

$$M = \frac{2EI\epsilon_{avg}}{D} \quad (3)$$

289 To obtain the profile of the bending moment along the monopile, an interpolation of the moment
290 calculated at each FBG level needed to be done. This was achieved by using fifth-order
291 polynomial fitting, which provided the best estimate of the measured data. Six coefficients in the
292 polynomial needed to be identified. The first three were determined from i) the bending moment
293 calculated at the first FBG level (i.e. at the ground level), ii) the shear force at the ground
294 surface calculated by dividing the zero-exponent coefficient by load eccentricity l_e , and iii) the
295 absence of soil reaction at the ground surface. The remaining coefficients were determined
296 from the best fit of the measured data presented as empty markers in Figure 8. Note that at the
297 monopile tip, no boundary condition was considered. At the ground level in both tests, the
298 maximum difference between the moment calculated by the FBG and that calculated by
299 multiplying load eccentricity with loads measured by the horizontal load cell was less than 0.2%.
300 This confirms the reliability of the FBGs used in this study. In both tests, J1g (Figure 8(a)) and
301 ID100g (Figure 8(b)), the moment increased with the depth up to approximately $1.5D$ below the
302 ground surface. Then, the moment gradually decreased to a very low value at $4.5D$. However,
303 the existence of a moment-related reaction at the monopile base is difficult to confirm.
304

305 4.2.3 Soil reactions

306 The first and second derivatives of the profiles of the bending moment yielded profiles of the
307 shear force and the horizontal soil reaction if the distributed moment along the monopile shaft
308 was negligible. Experimentally, this distributed moment was difficult to assess. However,
309 authors neglected it here based on work by Burd *et al.* (2020b). They conducted numerical
310 simulations similar to our tests in a saturated, dense, sandy medium by using a 1D finite
311 element model (calibrated on a 3D FEM) with $L/D = 6$. They obtained a resistance lower than
312 7% when considering only the lateral soil reactions compared with when all mechanisms were
313 considered. In this study, profiles of the shear force S and soil reaction p are plotted in Figure 8.
314 For the same horizontal load, S and p were similar in both tests. ID100g featured higher lateral
315 resistance than J1g.

316

317 4.2.4 Deflections

318 The monopile was modelled following Timoshenko's beam theory (i.e. shear strains within the
319 monopile were included). The profiles of its neutral axis of rotation θ (clockwise positive) and
320 deflection y were determined as follows:

$$\theta = -\frac{1}{EI} \int Mdz + \frac{S}{\kappa AG} - c_1 \quad (4)$$

$$y = \frac{1}{EI} \iint Mdz - \frac{M}{\kappa AG} + c_1z + c_2 \quad (5)$$

321 where Timoshenko's shear coefficient κ was equal to 0.9 (Faghidian, 2017), A is cross-sectional
322 area of the monopile, G is its shear modulus (see Table 3), and two integration constants c_1
323 and c_2 were obtained by using the monopile deflection measured by the top non-contact laser
324 displacement transducer and the deflection of the monopile at its rotation centre. The latter was
325 determined by finding the depth at which the soil reaction between two loading increments
326 remained constant (El Haffar, 2018). At this depth, the horizontal displacement of the monopile
327 remained constant between the two load increments.

328

329 Figure 8 also shows the normalised deflection of the monopile y/D and its neutral axis of rotation
330 θ . In contrast to the profiles S and p , those of y/D and θ in ID100g were lower than in J1g.
331 Figure 9 presents the normalised deflection profiles of the monopile above and below the
332 ground surface for both tests at four loading states (for M_G every 100 MN.m until 400 MN.m).
333 The depth at which no deflection was obtained corresponded to a distance of 18.75 m from the
334 ground surface, i.e. $z/D = 3.75$ or $z/L = 0.75$. This depth was close to the centre of rotation of the
335 monopile. The figure also shows monopile deflections measured by the bottom laser
336 displacement transducer (not used for the integration procedure). These measurements were
337 consistent with the deflection profiles obtained previously. The slight difference in case of the
338 ID100g test was due to uncertainties captured in case of small displacements.

339

340 4.2.5 Load transfer curves

341 The influence of the method of installation on the p - y curves at different depths (between $0.5D$
342 and $3D$) is shown in Figure 10. For small loading amplitudes, the p - y curves of the ID100g test
343 had stiffer responses than those of the J1g test. This tendency became less pronounced with
344 increasing loading. At the first level, $z = 0.5D$, the soil reactions reached the same plateau in
345 both tests. At deeper layers, this was difficult to determine as not enough displacements were
346 generated to reach a plateau.

347

348 The increase in the initial stiffness can be explained by an increase in horizontal stress along
349 the monopile shaft during in-flight installation compared with that in case of a jacked monopile.
350 Before the horizontal loading, the radial stress should be higher for ID100g. However, this
351 increase occurred because the in-flight driving was located in an area close to the monopile.
352 This is why for larger horizontal loading mobilizing the soil faraway, the difference in the soil
353 reaction decreased.

354 4.3 Quantitative comparison

355 In addition to the above qualitative comparisons, the effect of impact-driven installation on the
356 lateral response of the monopile was also determined based on two criteria. The first, $\theta_G = 0.5^\circ$,

357 was close to the limit state requirement of serviceability for a typical offshore wind turbine
358 (DNVGL, 2016). The second criterion, $y = 0.1D$ for different soil layers, represents the 'ultimate
359 limit state' corresponding to the conventional failure generally admitted for large displacements.

360

361 Table 4 summarises, for both tests, the secant stiffness defined at $\theta_G = 0.5^\circ$ for global curves
362 ($M_G - \theta_G$ and $H_G - y_G/D$ in Figure 6) and local curves ($p - y/D$ in Figure 10). For both global and local
363 analyses, the installation technique had a significant effect on the secant stiffness: multiplication
364 by 1.6 to 3 for 100g driving instead of 1g jacking.

365

366 The lateral resistances mobilised at $y = 0.1D$ are presented in Table 5. At the ground level, the
367 in-flight installation improved the lateral capacities (H_G and M_G) by 1.45, slightly higher than that
368 reported by Fan *et al.* (2019), who obtained a value of 1.31 for a $3.1D$ embedding into dry sand
369 with a relative density of 38% and $l_e = 3.8 D$. With regard to the local response of the monopile
370 at $0.1D$ in each layer, the soil reaction increased by 1.24 to 1.33. The in-flight installation
371 improved the soil reaction in deeper layers more significantly, but the effects of in-flight impact
372 driving were pronounced close to the monopile axis for a narrow range of horizontal
373 displacement.

374

375 Comparisons of the secant stiffness at $\theta_G = 0.5^\circ$ between the experimental $p - y/D$ curves K_{py}^{exp}
376 and those obtained from the standards K_{py}^{DNVGL} (DNVGL, 2016) are shown in Table 6. This
377 standard suggests an initial modulus of subgrade reaction of about 34 MN/m^3 at a frictional
378 angle of 38° . The experimental stiffnesses were lower than those predicted by the standards.
379 This phenomenon was more pronounced in deeper layers. However, with the in-flight impact
380 driving of the monopile, the results of the experiments were much closer to the standard.
381 Therefore, the lack of stiffness observed in centrifuge modelling was related to the effect of
382 installation and the use of clean, poured sand, which is different from the geological sand used
383 in situ. The DNVGL (2016) yielded results about 2.6 to 5.8 times higher for the J1g test, while
384 for ID100g, the DNVGL values were 1.2 to 2.8 times higher than the experimental ones.

385

386 For a large amplitude in case of a normalised displacement of $0.1D$, the DNVGL-mobilised
387 lateral resistances p^{DNVGL} were compared with those obtained from the experimental p - y/D
388 curves p^{exp} (Table 7). The results show that the experimental lateral resistances were similar to
389 those of the standards. For J1g, the DNVGL resistances were about 1.2 times higher, while for
390 ID100g, the standards resistances were slightly lower than the experimental results.

391 5 Conclusions

392 The set-up developed at the Gustave Eiffel University allows for the combination of the impact-
393 driven installation of a 50 mm monopile with a new miniature electro-mechanical hammer,
394 followed by horizontal monotonic loading in a centrifuge at 100g.

395

396 The global and local horizontal responses of the monopile were investigated for two methods of
397 installation—impact driving at 100g, and monotonically jacked installation at 1g—into water-
398 saturated Fontainebleau NE34 sand up to a depth of $5D$. No soil plugging was observed, which
399 enables an accurate comparison of the responses of the monopile under lateral loading. The
400 findings are as follows:

- 401 ▪ A set of two diametrically opposed FBGs, which measured normal strains within the
402 monopile, resisted the driving process at 100g. The optical fibres worked appropriately in
403 the subsequent lateral load tests. The bending moment calculated by using the force of the
404 horizontal actuator was in accordance with that measured by the FBGs at the ground level.
- 405 ▪ During horizontal loading, the compressive and tensile normal strains were asymmetric, as
406 has been reported by Li *et al.* (2020). Furthermore, the asymmetry was more significant at
407 the monopile base. This might have occurred due to strain localisation at the boundaries of
408 the monopile, as its slenderness ratio was too low to consider it to be a flexible beam.
- 409 ▪ The driven monopile better resisted overturning moments and forces, especially in case of
410 small loading amplitude. This enhancement decreased progressively as the resistance
411 increased until it stabilised at high loading amplitudes. These findings have also been
412 reported by Fan *et al.* (2019).

- 413 ▪ With regard to serviceability conditions ($\theta_G \leq 0.5^\circ$), the increase in secant stiffness was
414 highly pronounced in case of in-flight driving installation (3 times greater than in case of the
415 1g installation).
- 416 ▪ In case of the ultimate state condition ($y/D \sim 0.1$), an increase in the lateral capacity of the
417 in-flight driving installation was prominent (1.3 times higher).
- 418 ▪ The effect of impact driving was more localised in the vicinity of the monopile, and was
419 more pronounced for a narrow range of horizontal displacement. This may be owing to the
420 strong radial stress state induced during impact driving that was not present far from the
421 monopile.
- 422 ▪ The DNVGL (2016) predicted stiffness value 2.6 to 5.8 times higher than the experimental
423 ones for the J1g test. For the ID100g test, the DNVGL values were 1.2 to 2.8 times higher.
- 424 ▪ The ultimate resistance values of the DNVGL were similar to the experimentally mobilised
425 capacities for normalised displacement of $0.1D$ at a large amplitude.
- 426 Developing an electro-mechanical hammer requires ingenuity, time, and validation of the
427 relevant concepts from 1g progressively up to 100g. Nevertheless, it is important to model
428 impact-driven installation in the centrifuge as it clearly stiffens the soil–monopile interaction.
- 429 In future work, the authors will consider the effects of the embedding depth, the use of fluid with
430 scaled viscosity, and the blow rate on the lateral response of impact-driven monopiles.

431

432 **Acknowledgements**

433 This research study received state support from the National Research Agency under the
434 Investments for the Future Program (ANR-10-IEED-0006-08), and from the France Energies
435 Marines (SOLCYP+) and the Weamec (West Atlantic Marine Energy Community) through the
436 REDENV-EOL project. The authors thank Gustave Eiffel University and the Region Pays de la
437 Loire for financial support in the form of thesis grants. Finally, we are grateful to the centrifuge
438 team at Gustave Eiffel University (Stéphane Lerat, Alexandre Jagu, Patrick Gaudicheau, Alain
439 Néel, and Philippe Audrain) for their technical support in building the experimental device.

440

441 **References**

442 Abadie CN, Byrne BW and Houlsby GT (2019) Rigid pile response to cyclic lateral loading:

443 laboratory tests. *Géotechnique*, **69(10)**: 863–876, <https://doi.org/10.1680/jgeot.16.P.325>.

444 API (American Petroleum Institute) (2007) *API RP 2A-WSD: Recommended Practice for*
445 *Planning, Designing and Constructing Fixed Offshore Platforms - Working Stress Design*.
446 API, Washington, DC, USA.

447 Astley RJ (1992) *Finite Elements in Solids and Structures: An introduction*. Chapman & Hall,
448 London, UK.

449 Bayton SM, and Black JA (2016) The effect of soil density on offshore wind turbine monopile
450 foundation performance. In *Proceedings of 3rd European Conference on Physical*
451 *Modelling in Geotechnics*, Eurofuge, Nantes (Thorel L, Bretschneider A, Blanc M and
452 Escoffier S (eds)). IFSTTAR, Nantes, France, pp. 239–244. See
453 <https://www.issmge.org/uploads/publications/53/54/036-bayton%20&%20Black.pdf>
454 (accessed 01/06/2016).

455 Burd HJ, Beuckelaers WJAP, Byrne BW *et al.* (2020a) New data analysis methods for
456 instrumented medium-scale monopile field tests. *Géotechnique*, **70(11)**: 961–969,
457 <https://doi.org/10.1680/jgeot.18.pisa.002>

458 Burd HJ, Taborda DM, Zdravković L *et al.* (2020b) PISA design model for monopiles for offshore
459 wind turbines: application to a marine sand. *Géotechnique*, **70(11)**: 1048–1066,
460 <https://doi.org/10.1680/jgeot.18.P.277>.

461 Byrne BW, McAdam RA, Burd HJ *et al.* (2017) PISA: New design methods for offshore wind
462 turbine monopiles. In *Offshore Site Investigation and Geotechnics (OSIG) – Smarter*
463 *solutions for Future Offshore Developments: Proceedings of the 8th International*
464 *Conference*. Society for Underwater Technology, London, UK, vol. 1, pp. 142–161.

465 Byrne BW, McAdam RA, Burd HJ *et al.* (2020) Monotonic laterally loaded pile testing in a stiff
466 glacial clay till at Cowden. *Géotechnique*, **70(11)**: 1030–1047,
467 <https://doi.org/10.1680/jgeot.18.P.255>.

468 Choo YW, and Kim D (2016) Experimental development of the p-y relationship for large-
469 diameter offshore monopiles in sands: Centrifuge tests. *Journal of Geotechnical and*
470 *Geoenvironmental Engineering*, **142(1)**: 04015058,
471 [https://doi.org/10.1061/\(ASCE\)GT.1943-5606.0001373](https://doi.org/10.1061/(ASCE)GT.1943-5606.0001373).

472 De Nicola A (1996) *The performance of Pipe piles in sand*. Doctoral dissertation, University of

473 *Western Australia, Perth, Australia.*

474 De Nicola A and Randolph MF (1994) Development of a miniature pile driving actuator. In
475 *Centrifuge 94: Proceedings of the International Conference Centrifuge 94* (Leung CF, Lee
476 FH and Tan TS (eds)). Balkema, Rotterdam, the Netherlands, pp. 473–478.

477 De Nicola A and Randolph MF (1997) The plugging behavior of driven and jacked piles in sand.
478 *Geotechnique*, **47(4)**: 841–856, <https://doi.org/10.1680/geot.1997.47.4.841>.

479 DNVGL (Det Norske Veritas and Germanischer Lloyd) (2016) *Standard DNVGL-ST-0126:*
480 *Support structures for wind turbines, April 2016*. DNVGL, Høvik, Norway.

481 Doherty P, Igoe D, Murphy G *et al.* (2015) Field validation of fibre bragg grating sensors for
482 measuring strain on driven steel piles. *Geotechnique Letters*, **5(2)**: 74–79,
483 <https://doi.org/10.1680/geolett.14.00120>.

484 Dupla JC, Palix E, Damblans G *et al.* (2019) The ANR SOLCYP+ project for improving the
485 design of monopiles used as offshore wind turbines foundations. *Revue Française de*
486 *Géotechnique*, 158: article 4, <https://doi.org/10.1051/geotech/2019010> (in french).

487 Dyson GJ and Randolph MF (2001) Monotonic Lateral Loading of Piles in Calcareous Sand.
488 *Journal of Geotechnical and Geoenvironmental Engineering*, **127(4)**: 346–352,
489 [https://doi.org/10.1061/\(ASCE\)1090-0241\(2001\)127:4\(346\)](https://doi.org/10.1061/(ASCE)1090-0241(2001)127:4(346)).

490 El Haffar I (2018) *Physical modeling and study of the behavior of deep foundations of offshore*
491 *wind turbines*. Doctoral dissertation, Ecole Centrale de Nantes, Nantes, France. See
492 <https://www.theses.fr/2018ECDN0021> (accessed 01/01/2020).

493 Faghidian SA (2017) Unified formulations of the shear coefficients in Timoshenko beam
494 theory. *Journal of Engineering Mechanics*, **143(9)**: 06017013,
495 <https://doi.org/10.1680/jphmg.18.00028>.

496 Fan S, Bienen B and Randolph MF (2019) Centrifuge study on effect of installation method on
497 lateral response of monopiles in sand. *International Journal of Physical Modelling in*
498 *Geotechnics* **21(1)**: 40–52. <https://doi.org/10.1680/jphmg.19.00013>.

499 Fan S, Bienen B, and Randolph MF (2021a) Effects of Monopile Installation on Subsequent
500 Lateral Response in Sand. I: Pile Installation. *Journal of Geotechnical and*
501 *Geoenvironmental Engineering*, **147(5)**: 04021021,
502 [https://doi.org/10.1061/\(ASCE\)GT.1943-5606.0002467](https://doi.org/10.1061/(ASCE)GT.1943-5606.0002467).

503 Fan S, Bienen B and Randolph MF (2021b) Effects of Monopile Installation on Subsequent
504 Lateral Response in Sand. II: Lateral Loading. *Journal of Geotechnical and*
505 *Geoenvironmental Engineering*, **147(5)**: 04021022.
506 [https://doi.org/10.1061/\(ASCE\)GT.1943-5606.0002504](https://doi.org/10.1061/(ASCE)GT.1943-5606.0002504).

507 Garnier J (2001) Physical models in geotechnics. *Revue Française de Géotechnique*, 97: pp. 3–
508 29. <https://doi.org/10.1051/geotech/2001097003> (in french).

509 Garnier J and König D (1998) Scale effects in piles and nail loading tests in sand. In *Centrifuge*
510 *98: Proceedings of International conference Centrifuge 98* (Kimura T, Kusakabe O and
511 Takemura J (eds)). Balkema, Rotterdam, the Netherlands, vol. 1, pp. 205–210.

512 Garnier J, Gaudin C, Springman SM *et al.* (2007) Catalogue of scaling laws and similitude
513 questions in geotechnical centrifuge modelling. *International Journal of Physical Modelling*
514 *in Geotechnics*, **7(3)**: 01–23, <https://doi.org/10.1680/ijpmg.2007.070301>.

515 Kim BT, Kim NK, Lee WJ and Kim YS (2004) Experimental load-transfer curves of laterally
516 loaded piles in Nak-Dong River sand. *Journal of Geotechnical and Geoenvironmental*
517 *Engineering*, **130(4)**: 416–425. [https://doi.org/10.1061/\(ASCE\)1090-0241\(2004\)130:4\(416\)](https://doi.org/10.1061/(ASCE)1090-0241(2004)130:4(416))

518 Klinkvort RT (2012) Centrifuge modelling of drained lateral pile-soil response - Application for
519 offshore wind turbine support structures. Doctoral dissertation, Technical University of
520 Denmark, Lyngby, Denmark, See <https://core.ac.uk/reader/18600667>.

521 Klinkvort RT (2018) *Centrifuge monopile tests in sand. Factual report of laboratory testing*.
522 Norwegian Geotechnical Institute, Oslo, Norway.

523 Kutter BL (1994) Recent advances in centrifuge modelling of seismic shaking, state-of -the-Art
524 Paper. In *Proceedings of 3rd International Conference on recent advances in Geotechnical*
525 *Earthquake Engineering and Soil dynamics*. University of Missouri-Rolla, St. Louis, MO,
526 USA, vol. 2, pp. 927–942.

527 Levacher D, Morice Y, Favraud C and Thorel L (2008) *A review of pile drivers for testing in*
528 *centrifuge*. In *Journées Nationales Génie Côtier–Génie Civil No. 10 (2018): Sophia*
529 *Antipolis* (Levacher D and Gaufres P (eds)), pp. 573–584,
530 <https://doi.org/10.5150/jngcgc.2008.055-l>. Editions Paralia, Centre Français du Littoral,
531 Nantes, France.

532 Li Z, Thorel L and Blanc M (2020) Using FBGs to estimate the horizontal response of a

533 monopile in a geotechnical centrifuge. *International Journal of Physical Modelling in*
534 *Geotechnics*, **20(3)**: 164–174, <https://doi.org/10.1680/jphmg.19.00022>.

535 Mayall R (2019) *Monopile Response to Scour and Scour Protection*. Doctoral dissertation,
536 University of Oxford, Oxford, UK. See [https://ora.ox.ac.uk/objects/uuid:2886ac08-c59e-](https://ora.ox.ac.uk/objects/uuid:2886ac08-c59e-409d-8d60-6724443d8d1a)
537 [409d-8d60-6724443d8d1a](https://ora.ox.ac.uk/objects/uuid:2886ac08-c59e-409d-8d60-6724443d8d1a).

538 McAdam RA, Byrne BW, Houlsby, GT *et al.* (2020) Monotonic laterally loaded pile testing in a
539 dense marine sand at Dunkirk. *Géotechnique*, **70(11)**: 986–998,
540 <https://doi.org/10.1680/jgeot.18.pisa.004>

541 Remaud D (1999) *Piles subjected to lateral loading: Experimental study on group effect*.
542 Doctoral thesis, Ecole Centrale de Nantes, Nantes, France (in French). See
543 <https://www.theses.fr/1999NANT2109> (accessed 26/08/2021).

544 Rosquoet F, Thorel L, Garnier J and Canepa Y (2007) Lateral cyclic loading of sand-installed
545 piles. *Soils and foundations*, **47(5)**: 821–832. <https://doi.org/10.3208/sandf.47.821>.

546 Sieffert JG and Levacher D (1995) Scale effect analysis of piles driven in centrifuge. *Revue*
547 *française de géotechnique*, **70**, pp. 55–68. <https://doi.org/10.1051/geotech/1995070055> (in
548 French).

549 Ternet O (1999) *Reconstitution and Characterization of sand Massive: Application to centrifuge*
550 *and calibration chamber testing (in french)*. Doctoral thesis, Université de Caen
551 Normandie, Caen, France (in French). <https://www.theses.fr/1999CAEN2061> (accessed
552 26/08/2021).

553 Uesugi and Kishida (1986) Frictional resistance at yield between dry sand and mild steel. *Soils*
554 *and Foundations*, **26(4)**: 139–149. https://doi.org/10.3208/sandf1972.26.4_139.

555 Van Zeban JCB, Azua-Gonzalez C, Alvarez Grima M, Van't Hof C and Askarinejad A (2018)
556 Design and performance of an electro-mechanical pile driving hammer for geo-centrifuge.
557 In *Physical modelling in Geotechnics (ICPMG 2018)* (McNamara A, Divall S, Goodey R,
558 Taylor N, Stallebrass S and Panchal J (eds)). CRC Press/Balkema, London, UK, vol. 1,
559 pp. 469–473.

560

561 **Table and Figure Captions**

562 Table 1. Recap of hammers of the centrifuge (updated from Levacher *et al.*, 2008).

563 Table 2. Instrumentation of the experimental device.

564 Table 3. Geometric and mechanical characteristics of the model monopile.

565 Table 4. Experimental lateral secant stiffness at $\theta_G = 0.5^\circ$.

566 Table 5. Experimental lateral resistance at $y/D = 0.1$.

567 Table 6. p - y secant stiffness at $\theta_G = 0.5^\circ$; from the DNVGL (2016).

568 Table 7. Lateral resistance at $y/D = 0.1$; from the DNVGL (2016).

569

570 Figure 1. Experimental set-up: (a) schematic drawing; (b) photograph in the centrifuge basket.

571 Figure 2. (a) Monopile-driving hammer and (b) details of the hammering process.

572 Figure 3. Top-view photograph after lateral loading.

573 Figure 4. Instrumentation for the monopile: (a) photograph and longitudinal section of the

574 instrumented monopile. (b) transversal section at the level of optical fibres. FBG, fibre Bragg

575 Grating.

576 Figure 5. Driving curve (number of blows n) and cumulative energy (ξ^N and ξ) at the prototype

577 scale plotted against the normalised settlement of the monopile.

578 Figure 6. At ground-level: (a) the bending moment plotted against rotation ($M_G - \theta_G$), (b) the

579 horizontal load plotted against normalized deflection ($H_G - y_G/D$), (c) the monopile rotation plotted

580 against normalised displacement ($\theta_G - y_G/D$).

581 Figure 7. Distribution of normal strains along the monopile for four horizontal loading states

582 corresponding to an increment of 100 MN.m in the ground-level bending moment.

583 Figure 8. Profiles of deflection, rotation, bending moment, and shear force of the monopile, and

584 the soil reactions for the (a) J1g test and (b) ID100g test. Four cases of loading were considered

585 at the prototype scale: $M_G = 100, 200, 300, \text{ and } 400 \text{ MN.m}$.

586 Figure 9. Deflection of the monopile above and below the ground level for the (a) J1g test and

587 (b) ID100g test.

588 Figure 10. Soil reaction plotted against the normalised monopile deflection for (a) J1g and (b)

589 ID100g tests.

Table 1. Recap of hammers of the centrifuge (updated from Levacher et al., 2008).

Hammer type	<i>L/D</i>	g-level	Ram mass (g)	Drop height (mm)	Frequency (Hz)	References
Pneumatic	9.4	100	70	0 – 20	20	De Nicola and Randolph (1994)
Electro-magnetic	25	50	40	20	–	Sieffert and Levacher (1995)
Electro-mechanical	2.9	50	220	40 – 55	35	Van Zeban <i>et al.</i> (2018)
Pneumatic	3.1	100	50	17	5	Fan <i>et al.</i> (2019)

Table 2. Instrumentation of the experimental device.

Sensor name	Location	Range	Linearity
Displacement	Hydraulic actuator	300 mm	0.01%
Displacement	Electro-mechanical actuator	150 mm	0.1%
Vertical laser disp.	Hammer housing	100 mm	0.3%
Potentiometric disp.	Inside the monopile	104 mm	0.1%
2 Horizontal laser disp.	In front of the electric actuator	120 mm	0.1%
Force	Hydraulic actuator	25 kN	0.2%
Force	Electro-mechanical actuator	5 kN	0.75%

Table 3. Geometric and mechanical characteristics of the model monopile.

Parameter	Model
D (m)	0.05
E (GPa)	72.5
EI (N·m ²)	7.7×10^3
G (GPa)	27.2
L (m)	0.25
I (m)	0.525
I_e (m)	0.25
t (m)	0.0025

Table 4. Experimental lateral secant stiffness at $\theta_G = 0.5^\circ$.

Secant Stiffness	z	Units	Test		Δ [%]
			J1g	ID100g	
k_{M_θ}	0	MN.m	337	541	61
$k_{H_{y/D}}$	0	MN	259	553	114
$k_{p_{y/D}}$	0.5D	MN/m	30	90	197
	1D	MN/m	65	198	204
	1.5D	MN/m	105	327	211
	2D	MN/m	151	482	219
	2.5D	MN/m	204	656	222
	3D	MN/m	266	824	210

Table 5. Experimental lateral resistance at $y/D = 0.1$.

Load/reaction	z	Units	Test		Δ [%]
			J1g	ID100g	
M_G	0	MN.m	355	515	45
H_G	0	MN	14.2	20.6	45
p	0.5D	MN/m	1.48	1.84	24
	1D	MN/m	3.11	3.97	27
	1.5D	MN/m	4.81	6.32	32
	2D	MN/m	6.57	8.75	33

Table 6. p - y secant stiffness at $\theta_G = 0.5^\circ$; from the DNVGL (2016).

z	K_{py}^{DNVGL} (MN/m)		$K_{py}^{DNVGL} / K_{py}^{exp}$	
	J1g	ID100g	J1g	ID100g
0.5D	79	112	2.6	1.2
1D	214	324	3.3	1.6
1.5D	406	649	3.9	2.0
2D	647	1077	4.3	2.2
2.5D	907	1566	4.4	2.4
3D	1539	2310	5.8	2.8

Table 7. Lateral resistance at $y/D = 0.1$; from the DNVGL (2016).

z	p^{DNVGL} (MN/m)		p^{DNVGL} / p^{exp}	
	J1g	ID100g	J1g	ID100g
<i>0.5D</i>	1.74	1.74	1.2	0.9
<i>1D</i>	3.85	3.85	1.2	1.0
<i>1.5D</i>	5.85	5.85	1.2	0.9
<i>2D</i>	7.23	7.23	1.1	0.8

Figure 1. Experimental set-up: (a) schematic drawing; (b) photograph in the centrifuge basket.

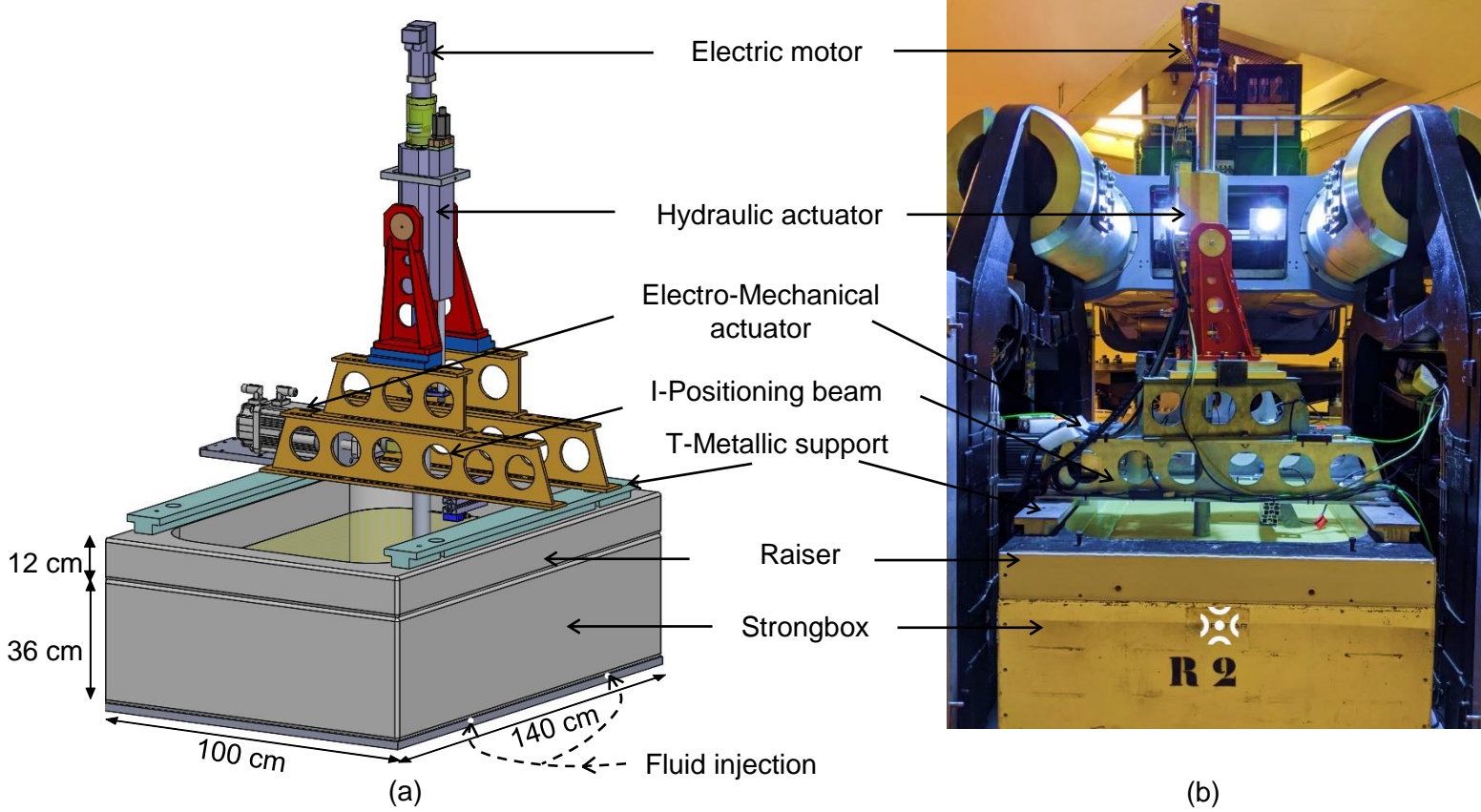


Figure 2. (a) Monopile-driving hammer and (b) details of the hammering process.

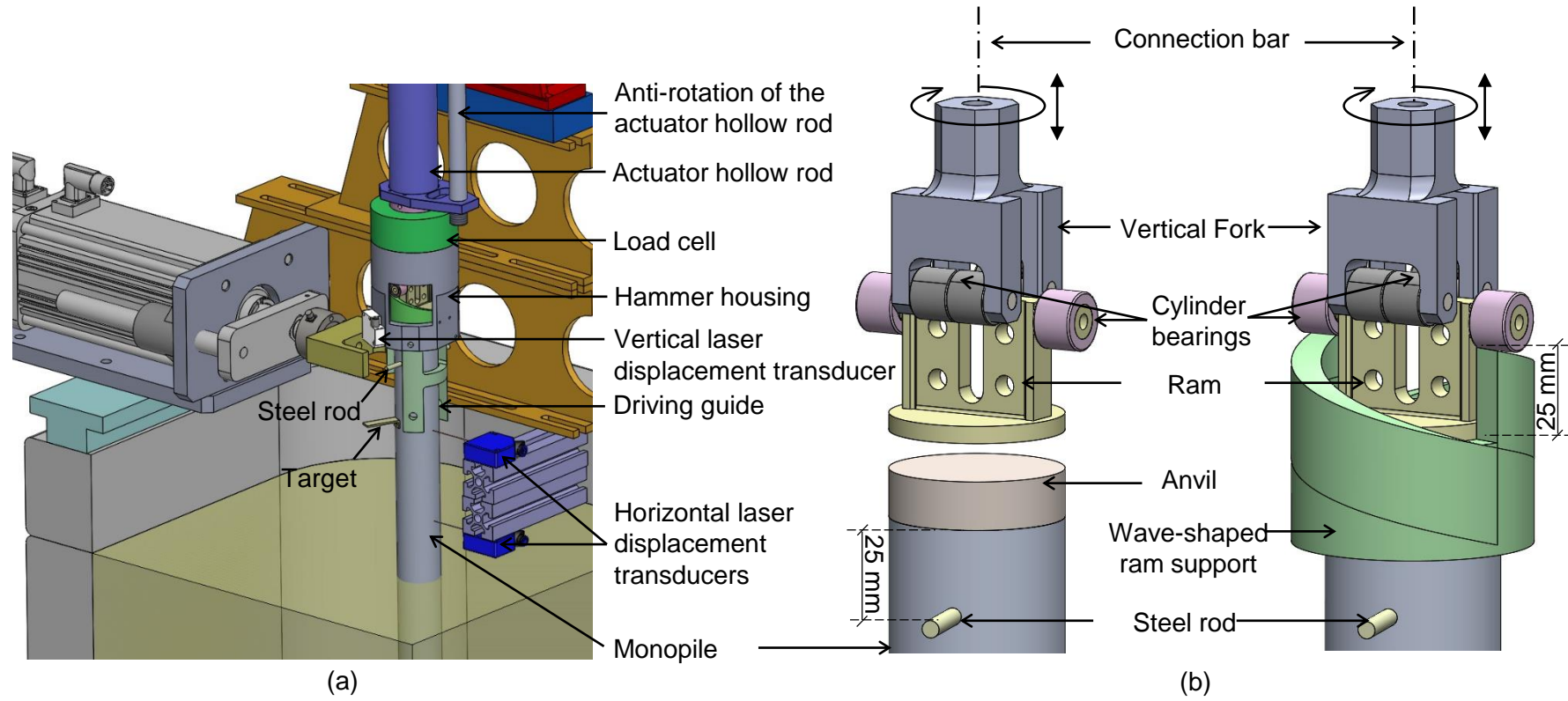


Figure 3. Top-view photograph after lateral loading.

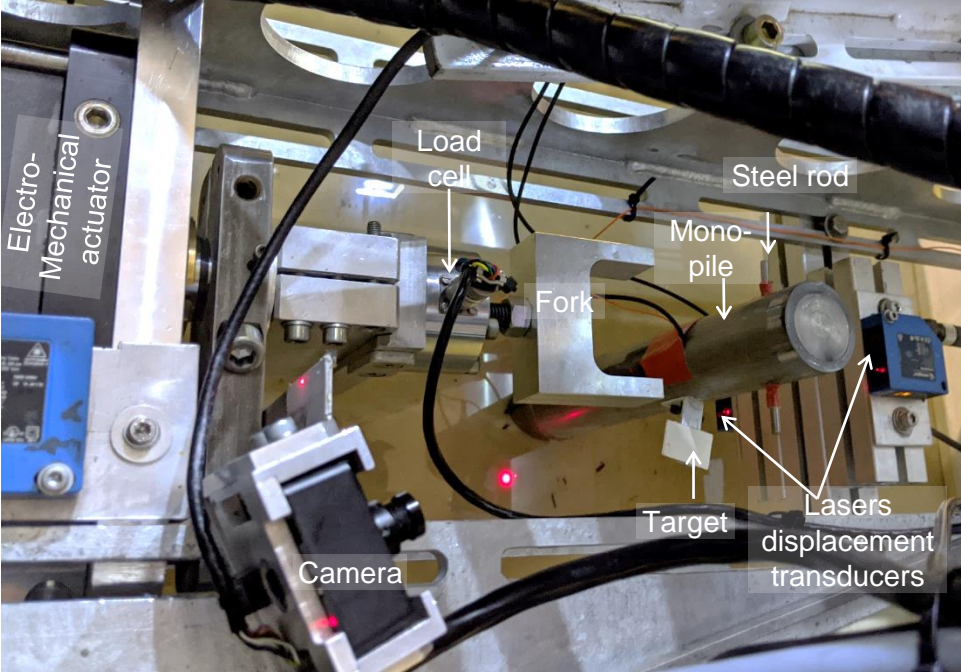


Figure 4. Instrumentation for the monopile: (a) photograph and longitudinal section of the instrumented monopile; (b) transversal section at the level of optical fibres. FBG, fibre Bragg Grating

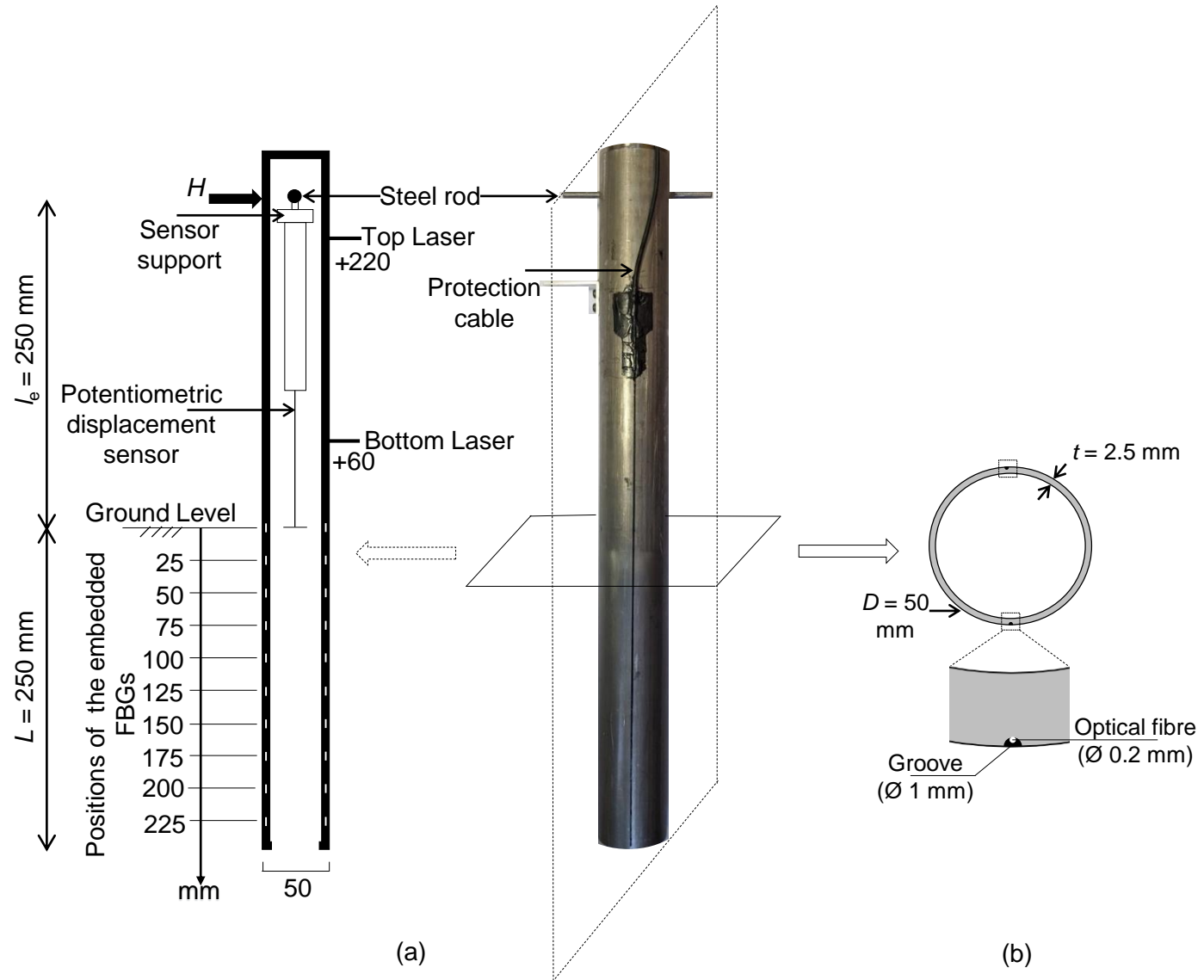


Figure 5. Driving curve (number of blows n) and cumulative energy (ξ^N and ξ) at the prototype scale plotted against the normalised settlement of the monopile.

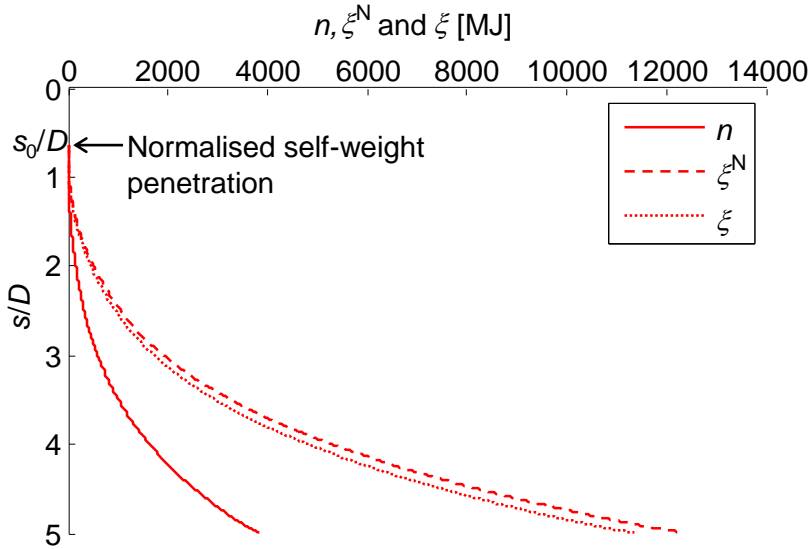
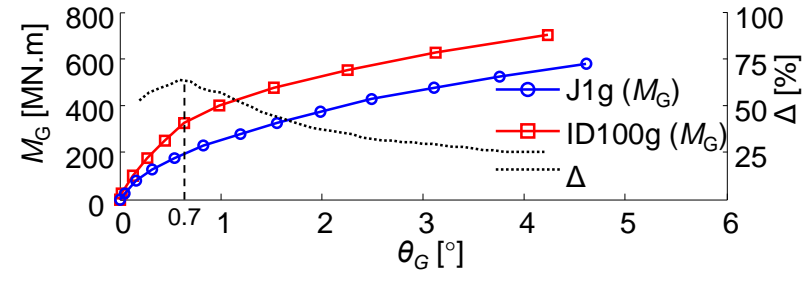
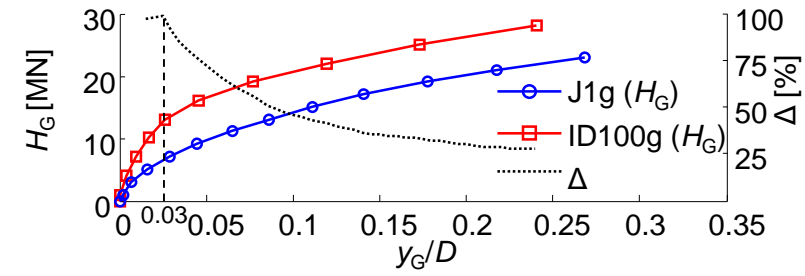


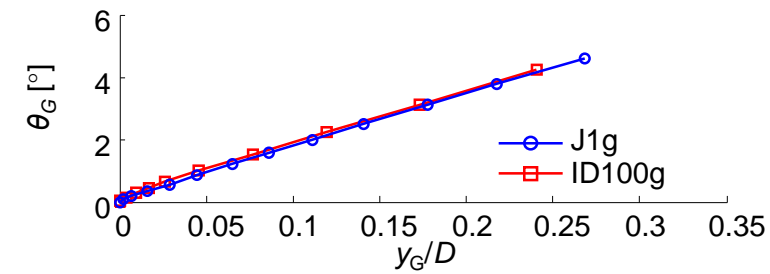
Figure 6. At ground-level: (a) the bending moment plotted against rotation ($M_G-\theta_G$), (b) the horizontal load plotted against normalized deflection (H_G-y_G/D), (c) the monopile rotation plotted against normalised displacement (θ_G-y_G/D).



(a)



(b)



(c)

Figure 7. Distribution of normal strains along the monopile for four horizontal loading states corresponding to an increment of 100 MN.m in the ground-level bending moment.

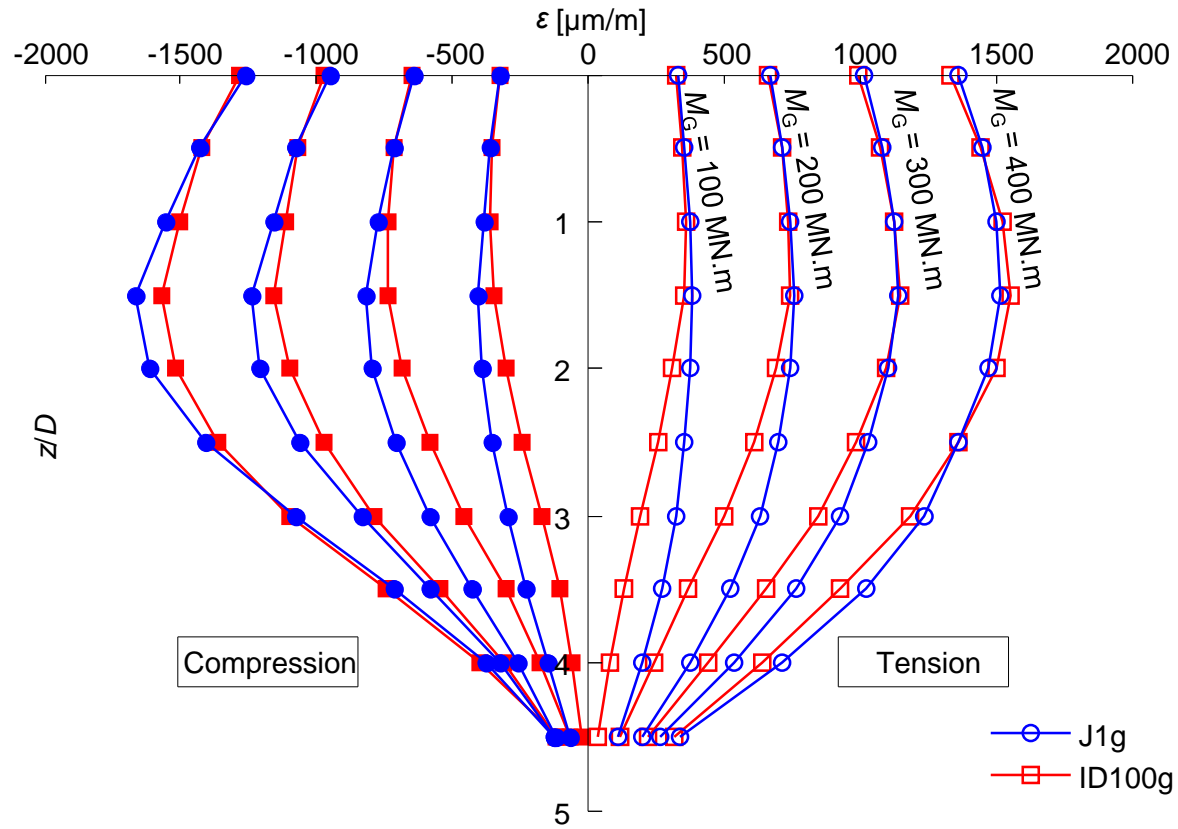


Figure 8. Profiles of deflection, rotation, bending moment, and shear of the monopile, and the soil reactions for the (a) J1g test and (b) ID100g test. Four cases of loading were considered at the prototype scale: $M_G = 100, 200, 300,$ and 400 MN.m.

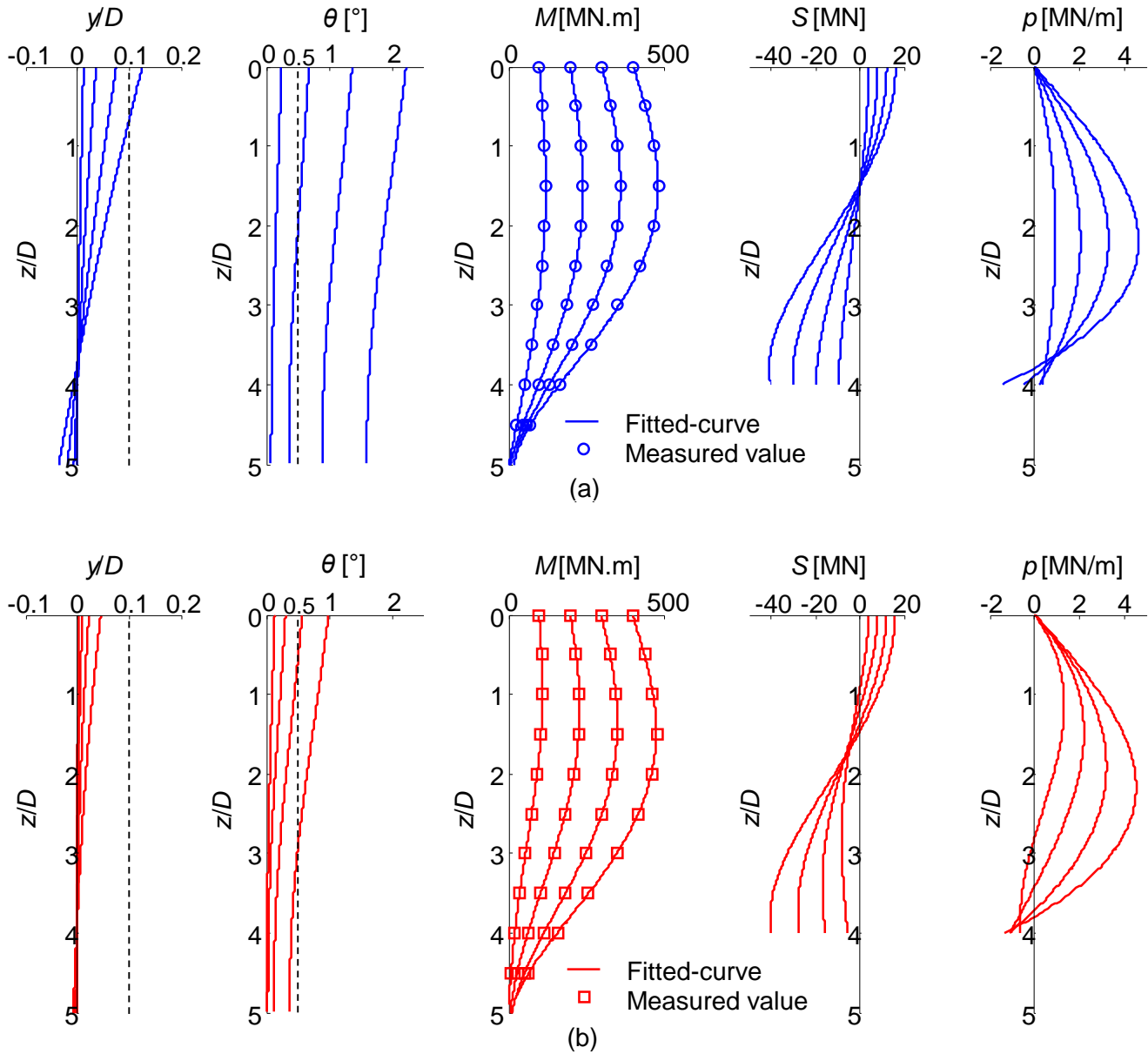
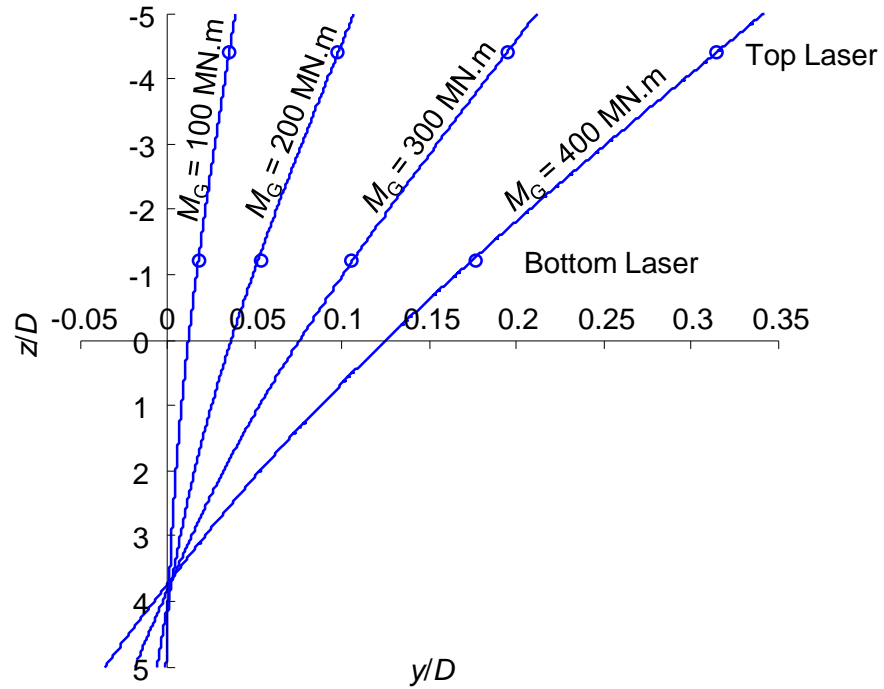
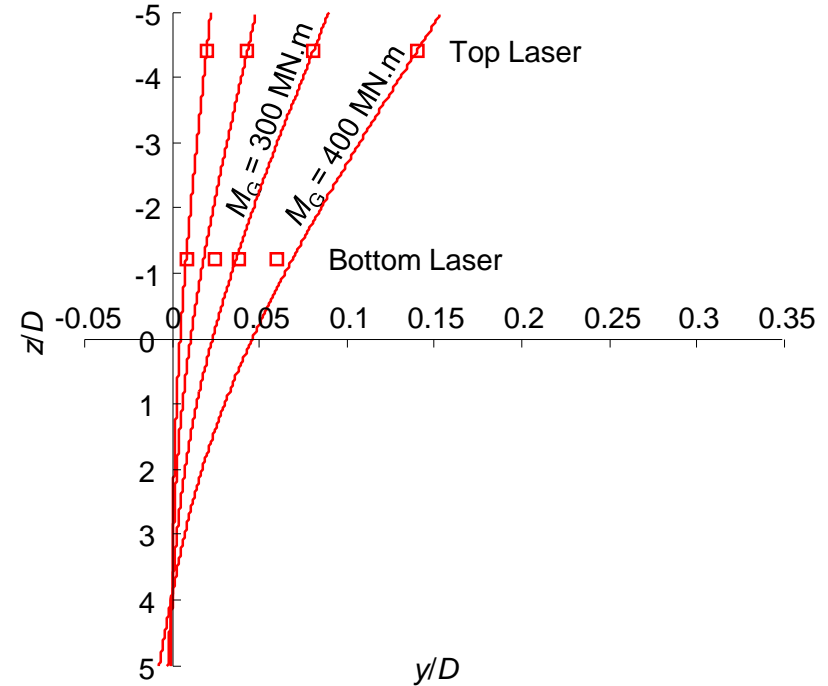


Figure 9. Deflection of the monopile above and below the ground level for the (a) J1g test and (b) ID100g test.

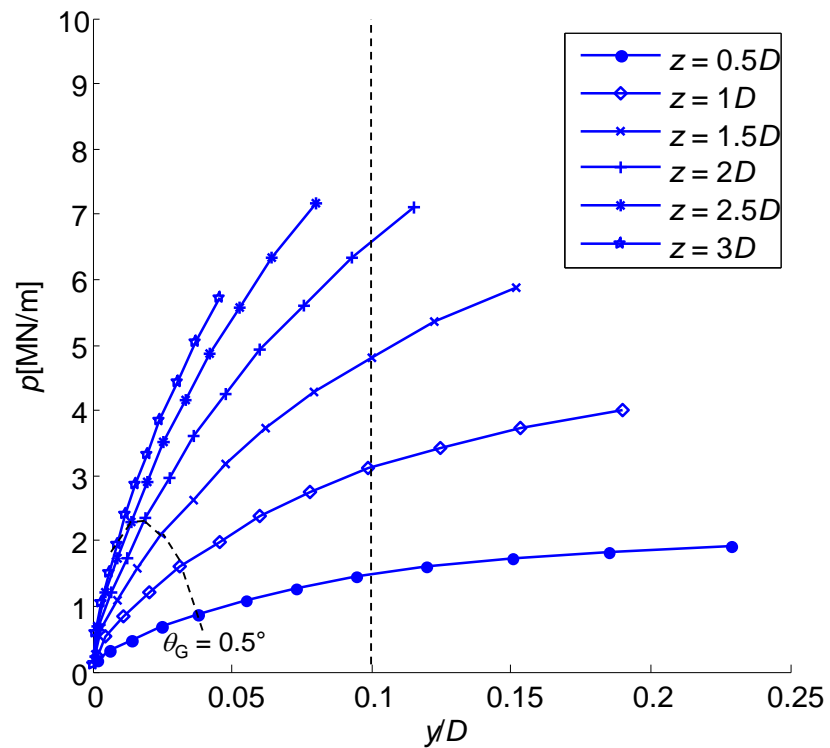


(a)

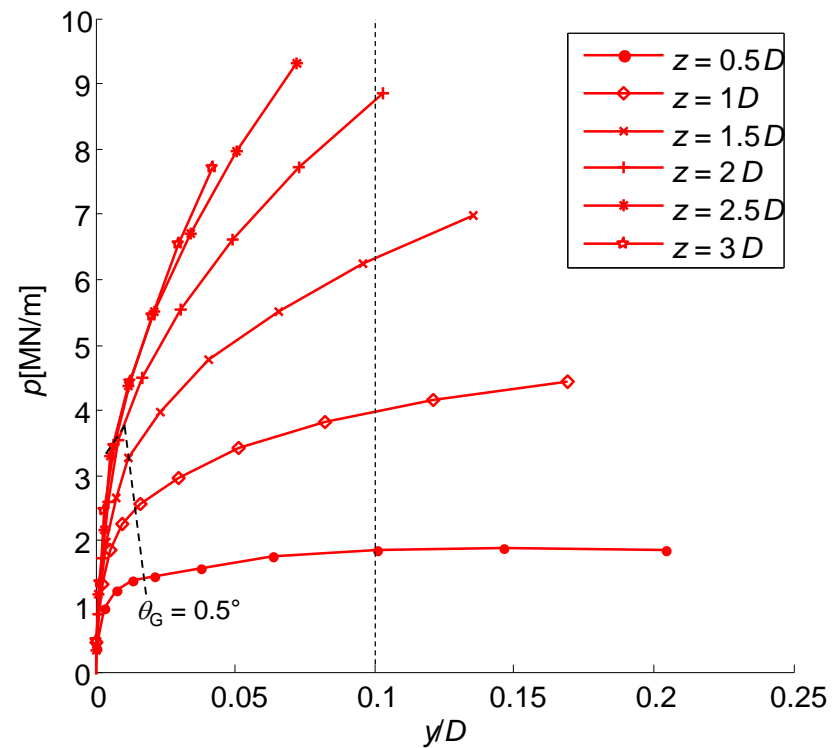


(b)

Figure 10. Soil reaction plotted against the normalised monopile deflection for (a) J1g and (b) ID100g tests.



(a)



(b)